Isolating the effects of moisture entrainment on convectively coupled equatorial waves in an aquaplanet GCM

Article

Published Version

Isolating the Effects of Moisture Entrainment on Convectively Coupled Equatorial Waves in an Aquaplanet GCM

SIMON C. PEATMAN, JOHN METHVEN, AND STEVEN J. WOOLNOUGH

National Centre for Atmospheric Science, Department of Meteorology, University of Reading, Reading, United Kingdom

(Manuscript received 29 March 2018, in final form 20 June 2018)

ABSTRACT

The rate of humidity entrainment in the convective parameterization scheme in a general circulation model affects the simulation of convectively coupled waves. However, it is unclear whether this is caused directly by the effects of entrainment on waves or indirectly through associated impacts such as on the basic state. Therefore, using an aquaplanet model, we employ a novel framework in which we entrain a weighted average of the resolved humidity field and a prescribed zonally symmetric field, with the weighting controlled by a decoupling parameter. Hence, we can vary the entrainment rate of basic-state humidity independently of the entrainment of humidity perturbations, simultaneously minimizing changes in the basic state. Thus, we isolate the effect of moisture entrainment on the waves. Enhancing the entrainment rate increases spectral power over all zonal wavenumbers and frequencies, with an increase in the ratio of eastward-to-westward power. The Kelvin wave speed decreases as entrainment increases, which can be partially accounted for by an associated change in basic-state humidity. Increasing the decoupling parameter reduces spectral power in Kelvin waves relative to the background, with only long waves still prominent when entrainment is almost fully decoupled from the resolved moisture field, suggesting the wave structure in humidity is required for convection to organize into short-wave structures. For long waves, the increase in the ratio of eastward-to-westward power as entrainment rate increases cannot be explained by the changes in the coupling with the wave structure in humidity but is consistent with the changes in the basic state.

1. Introduction

Convectively coupled waves, such as equatorial waves and African easterly waves (AEWs), play a key role in the organization of tropical convective precipitation (Kiladis et al. 2006; Hall et al. 2006; Kiladis et al. 2009). They are therefore of particular importance for forecasting in the tropics and understanding the distribution of tropical convection in climate simulations generally.

One important class of such waves is equatorial Kelvin waves, which propagate eastward with a phase speed of around 15–25 $\mathrm{m\,s^{-1}}$ with associated organized convection $\sim 10^3$ km across (Straub and Kiladis 2002; Mounier et al. 2007; Mekonnen et al. 2008). Over Africa, their modulation of convection is on the same order of magnitude as that by AEWs (Mounier et al. 2007; Janicot et al. 2008). It has also been proposed that they trigger AEWs (Ventrice and Thorncroft 2013), play a role in tropical cyclogenesis (Schreck and Molinari 2011), and can affect the onset date of the boreal summer West African monsoon (Cornforth 2013). Equatorial Kelvin and Rossby waves form the Matsuno–Gill response to diabatic heating in the tropics (Matsuno 1966; Gill 1980) and are believed to play a role in the initiation and propagation of the Madden–Julian oscillation (MJO; e.g., Matthews 2000; Zhang 2005; Haertel et al. 2015).

However, convectively coupled tropical waves and their related activity tend to be poorly simulated in numerical weather prediction (e.g., Vitart et al. 2007; Agustí-Panareda and Beljaars 2008) and climate models (e.g., Lin et al. 2006). Moreover, the basic equatorial wave theory (e.g., Matsuno 1966; Gill 1980; Holton 2004) inadequately represents the conditions under which waves propagate and couple to convection. For example, a resting mean state is assumed, so the theory does not account for meridional or vertical shear, which would cause tilt in the wave structures. The effects of latent heat release and cloud–radiative interaction are also not included.

Notwithstanding these shortcomings, the dry theory has reasonable success in predicting the waves' observed

Corresponding author: Dr. Simon Peatman, s.peatman@reading.ac.uk

DOI: 10.1175/JAS-D-18-0098.1

horizontal structures. Yang et al. (2003) demonstrated that observational and reanalysis data project strongly onto the theoretically derived structures (e.g., Yang et al. 2007a), but there are differences between observations and the basic dry theory. For example, in the upper troposphere, higher-order structures appear in eastward-propagating disturbances, including a meridional wind component (Yang et al. 2007b). In the eastern hemisphere, the observed convective maximum is approximately collocated with the maximum lower-tropospheric westerlies, and in the western hemisphere, it is centered between the lower-tropospheric westerlies and divergence maxima (Yang et al. 2007a), but in the theoretical dry dynamics, the maximum ascent is collocated with the convergence maximum.

Further mechanisms proposed to model the observed features of equatorial waves, particularly MJO propagation, include wave–conditional instability of the second kind (CISK; e.g., Hayashi 1970; Lindzen 1974; Lau and Peng 1987). In a CISK parameterization, heating depends on vertical velocity or large-scale low-level convergence, on the assumption this is enough to overcome convective inhibition by lifting moist, warm air to the level of free convection. In wave-CISK, this convergence may be provided by waves such as gravity, Kelvin, Rossby, or mixed Rossby–gravity waves. However, as discussed above, it is often unrealistic for convection to be collocated with the maximum in lower-troposphere convergence. Furthermore, this model suffers from the so-called wave–CISK catastrophe, a tendency for convection to collapse down to the smallest possible horizontal scale (Dunkerton and Crum 1991; Crum and Dunkerton 1992; Matthews and Lander 1999).

Improvements to convectively coupled waves in models will likely require a better understanding of the underlying processes. Here, we investigate the effect of the rate of moisture entrainment and detrainment on the waves. This is motivated in part by previous studies, described below, that have found an impact of moisture sensitivity and, specifically, entrainment and detrainment rate on the spatiotemporal distribution of convection, including the simulation of the MJO.

Hirota et al. (2014) showed that, in experiments with the Model for Interdisciplinary Research on Climate, version 5 (MIROC5), entrainment acts to increase both spatial and temporal variability in convection. The spatial variability arises as entrainment causes convection to be favored in regions of high humidity and ascent and suppressed in regions of low humidity and subsidence; and the temporal variability arises as congestus clouds moisten the midtroposphere, with high precipitation amounts occurring only once sufficient moisture becomes available. A model intercomparison study by Kim et al. (2014) showed the relationship between rainfall rate and the vertical relative humidity profile is strongly linked to models' ability to simulate the MJO, with a more realistic MJO in models with a stronger sensitivity of convection to moisture. Tokioka et al. (1988) showed that in an Arakawa–Schubert convection scheme, imposing a minimum value of cumulus entrainment rate was necessary to have an MJO.

Bechtold et al. (2008) found changes to the European Centre for Medium-Range Weather Forecasts (ECMWF) model, including making the entrainment rate proportional to environmental relative humidity, were responsible for improvements when forecasting synoptic to decadal time scales. This included a more realistic spectrum of convectively coupled equatorial waves and an MJO that maintains a more realistic amplitude. It was further shown by Hirons et al. (2013a,b) that this change in the representation of entrainment, by increasing the sensitivity of deep convection to the environmental humidity, alters the relationship between humidity and precipitation. Entrainment increases in dry columns, thus terminating convective plumes at a lower altitude and increasing the amount of cumulus congestus. The congestus clouds moisten the midtroposphere, priming the atmosphere for deep convection. This control on the transition to deep convection is important in the interaction between convection and large-scale waves.

Klingaman and Woolnough (2014) showed that enhancing the rate of deep- and midlevel entrainment in the Met Office Unified Model (MetUM) by 50% increases MJO activity almost to observed levels (except in the Maritime Continent). Furthermore, model forecast skill, measured by correlation of the real-time multivariate MJO (RMM; Wheeler and Hendon 2004) indices in hindcasts versus observations, improves from 12 to 22 days. They hypothesized that this is because increasing the entrainment rate tends to cause more shallow convection, which removes instability less efficiently. Therefore, instability can build up over a longer, more realistic time scale. However, changing the entrainment rate also has an impact on the model basic state. For example, Bush et al. (2015) showed that increasing the entrainment rate has an impact on regional feedbacks, which can affect model biases in the South Asian summer monsoon, and Möbis and Stevens (2012) and Oueslati and Bellon (2013) each demonstrated the sensitivity of organized tropical convection to the entrainment rate, particularly in the intertropical convergence zone (ITCZ), with enhanced entrainment favoring a single rather than double ITCZ.

Kang et al. (2013) used an aquaplanet experiment with various sea surface temperature (SST) profiles to

investigate the relative power of equatorial Kelvin and Rossby waves as a function of the broadness of the equatorial SST peak and its associated humidity distribution. A broader peak triggers the Rossby mode more strongly by increasing off-equatorial moisture convergence and altering static stability. This change in ITCZ structure and humidity in response to a changing SST profile is similar to that from changing entrainment. Following Klingaman and Woolnough (2014), in this study, we increase the rate of moisture entrainment for deep- and midlevel convection in the MetUM relative to a control case, and the effect on convectively coupled equatorial waves is diagnosed. Given the findings of Kang et al. (2013), a reasonable hypothesis is that as entrainment rate varies, associated changes in the basic state can account for any changes in convectively coupled waves as opposed to changes in the waves being directly due to changes in the wave moisture entrainment.

To investigate this, a novel framework is implemented in the convection scheme in which the basic-state humidity and humidity perturbations can be entrained at different rates. A zonally symmetric aquaplanet is used since this provides an idealized setup in which to investigate the effects of entrainment without the complication of spatial variations in the surface boundary condition, for example, due to orography or coastlines. Hence, wave propagation is uniform, and the analysis is made simpler as all longitudes are equivalent. Of course, in an idealized setup, the waves may have slightly different structures to those in reality, but a simplified setup such as this is ideal for examining the effect of entrainment in a straightforward manner.

The model is described in section 2 and the new entrainment framework defined in section 3. Results are presented in section 4 and conclusions in section 5.

2. Model description

MetUM, version 8.2, with the New Dynamics dynamical core, was used with the Global Atmosphere, version 3 (GA3), configuration (Walters et al. 2011). The latter study showed that, during boreal winter in the Pacific, there is a wet bias in the ITCZ and South Pacific convergence zone and a dry bias on the equator, as is indicative of a double-ITCZ bias. Bush et al. (2015) showed that the June–August basic state of this version of the MetUM is sensitive to increasing entrainment, and that while increasing the entrainment rate improved regional aspects of the tropical Indian Ocean and west Pacific precipitation, the overall mean state of this region was degraded. Klingaman and Woolnough (2014) showed that an earlier configuration [Global Atmosphere, version 2 (GA2)] had an improved simulation of the MJO with increased entrainment.

The MetUM uses a mass flux convective parameterization based on Gregory and Rowntree (1990), of which version 4A was used here with modifications as described in section 3. The model was run at N96 resolution (1.25° latitude × 1.875° longitude; approximately 200-km grid spacing at the equator) with 85 vertical levels; 3.5-yr integrations were performed, with the first 6 months discarded as spinup time. An aquaplanet setup was used with fixed, zonally symmetric SST. The dependence on latitude ϕ of SST was the "control" case from the Aqua-Planet Experiment (APE; Blackburn and Hoskins 2013):

$$\mathrm{SST}(^{\circ}\mathrm{C}) = \begin{cases} 27\left[1 - \sin^2\left(\dfrac{3\phi}{2}\right)\right], & 60^{\circ}\mathrm{S} < \phi < 60^{\circ}\mathrm{N} \\ 0, & \text{otherwise} \end{cases}. \tag{1}$$

In the standard (control configuration) convection scheme, the moisture entrained into a convective plume is

$$E_C = \varepsilon q^e M, \tag{2}$$

where ε is the control entrainment rate, q^e is the environmental (i.e., resolved) specific humidity, and M is the convective updraft mass flux. For deep- and midlevel convection, ε varies vertically as

$$\varepsilon(z) = 4.05\frac{p(z)\rho(z)g}{p_0^2}, \tag{3}$$

where z is height, p is pressure, ρ is density, g is acceleration due to gravity, and p_0 is surface pressure.

For shallow convection, the entrainment rates are specified based on the similarity theory of Grant and Brown (1999) and are not modified in this study. For deep and midlevel convection, we define a factor f that multiplies ε so the entrained moisture becomes

$$E_f = f\varepsilon q^e M. \tag{4}$$

We investigate the cases $f = 1.5$ and $f = 2.0$, in comparison with the control $f = 1.0$.

3. Experimental setup

a. Modifications to model entrainment

To isolate the role of moisture entrainment from other impacts of changing entrainment, we begin by partitioning q^e:

$$q^e(\lambda,\phi,z,t) = \overline{q}(\phi,z) + q'(\lambda,\phi,z,t)\,, \tag{5}$$

where λ is longitude, t is time, $\overline{q}$ is the basic-state specific humidity, and q' the perturbation from that basic state (i.e., the moisture within the wave). Since the prescribed SST is zonally symmetric, we define the basic state as the time and zonal mean.

As explained in section 1, we aim to separate the direct effect of changing moisture entrainment within a wave from other indirect impacts of varying f. Hence, we construct a new framework with the entrainment rate of q' held fixed while the entrainment rate of $\overline{q}$ (and basic-state temperature and momentum) varies with f. Therefore, we can investigate whether changes in wave activity require coupling with moisture in the wave dynamics or whether they arise through waves drawing on the basic state and wave–mean flow interaction. Hence, we seek to modify moisture entrainment rate such that

$$\tilde{E}_f \approx f\varepsilon\overline{q}M + \varepsilon q'M\,. \tag{6}$$

This is approximately achieved by modifying the moisture entrainment to entrain humidity $q + \Delta q$ instead of q when performing deep- or midlevel convection so that (4) becomes

$$\tilde{E}_f = f\varepsilon(q^e + \Delta q)M\,, \tag{7}$$

where we define

$$\Delta q = \alpha(q^c - q^e)\,. \tag{8}$$

Here, q^c is a specific humidity climatology that varies with latitude and height only and is prescribed; α is the decoupling parameter, which takes a value from 0 to 1 inclusive; $\alpha = 0$ is the fully coupled (control) case in which we entrain environmental humidity only, as normal. With $0 < \alpha < 1$, the entrainment is partially decoupled from the environment as we entrain a weighted sum $\alpha q^c + (1-\alpha)q^e$ of the humidities. With $\alpha = 1$, the decoupling is absolute as we entrain q^c only. Substituting (5) and (8) into (7) yields

$$\tilde{E}_f = f\varepsilon[\alpha q^c + (1-\alpha)\overline{q} + (1-\alpha)q']M\,. \tag{9}$$

Consider the case of nonzero α. If the q^c we prescribe is $\overline{q}$ from a previous model run that had the same f and had $\alpha = 0$, then we hypothesize that, unless entrainment of q' has a major effect on basic-state humidity, our model run with the modified scheme has

$$\overline{q} \approx q^c\,. \tag{10}$$

Substituting this into (9) yields an expression for the new amount of moisture entrained:

$$\tilde{E}_f \approx f\varepsilon\overline{q}M + f\varepsilon(1-\alpha)q'M\,. \tag{11}$$

Therefore, by comparison with (6), to entrain the basic state at the enhanced rate $f\varepsilon$ but the perturbations at the control rate ε, we require

$$\alpha = 1 - \frac{1}{f}. \tag{12}$$

This is implemented in the MetUM as described in section a of the appendix.

After convecting, the MetUM convection scheme calculates the effect on the environment and adjusts the resolved humidity q^e accordingly. When $\alpha = 0$, moisture is entrained from the environment, which has no effect on the environmental specific humidity, so we do not need to make any further adjustment. However, when $\alpha \neq 0$, we entrain air with different properties to q^e. To ensure conservation of moisture, Δq entrained in (7) has to be accounted for in the effect of convection on resolved scales. Details are given in section b of the appendix. The result, shown in (A9), is that the drying of q^e (due to subsidence, compensating for the updraft in the plume) is partially offset in moist environments and increased in dry environments.

b. Integrations performed and their interpretation

The experiment proceeds as follows, with model integrations shown in parameter space in Fig. 1. First, we vary f (holding $\alpha = 0$) to investigate the changes to the basic state and convectively coupled wave modes as the entrainment rate changes. As f increases, we are increasing the rate of entrainment of both the basic state and perturbations of humidity (and also of temperature and momentum). We then vary α to investigate the effect of decoupling entrained moisture from the wave structure. For fixed f, as α increases, the rate of entrainment of humidity perturbations decreases, but the rate of entrainment of the basic-state humidity is approximately fixed [(11)].

As explained above, we are particularly interested in the cases when $\alpha = 1 - 1/f$. For any given $f \neq 1$, we wish to compare the $\alpha = 1 - 1/f$ case to the $\alpha = 0$ case (where q^c came from the $\alpha = 0$ case with the same value of f).

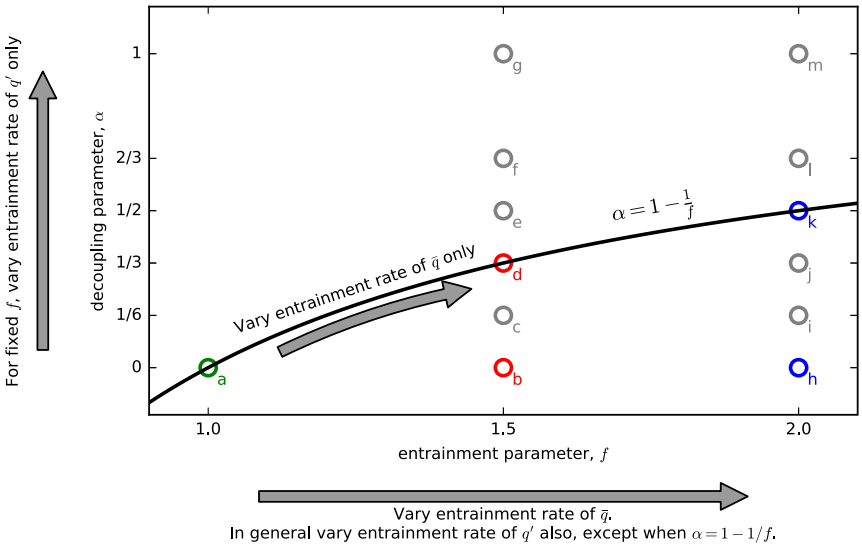

FIG. 1. The 13 experiments performed, each represented by a circular marker in parameter space for the entrainment (f) and decoupling (α) parameters, with colored circles indicating the cases $\alpha = 0$ and $\alpha = 1 - 1/f$. Labeled arrows indicate the effect on specific humidity q when the values of f and α vary. Letters indicate the associated panels in Figs. 8 and 10. The curve $\alpha = 1 - 1/f$ is shown in black, along which the entrainment of moisture within a wave q' is held at the control rate even as the entrainment of basic-state moisture $\overline{q}$ varies with f.

If the experiments with these two values of α give a similar result, we know that changes in convectively coupled wave activity as f changes do not result from changes to entrainment of perturbation moisture. This is because the two cases entrain humidity perturbations at a different rate (see Table 1) yet give the same result. Instead, the changes would be attributable to other impacts of varying f—for example, changes to the mass flux profile and entrainment of temperature, which may affect the vertical profile of diabatic heating, moisture, and momentum tendencies resulting from convection. Conversely, if the $\alpha = 1 - 1/f$ case gives a similar result to ($f = 1.0$, $\alpha = 0$), changes to the wave activity with changing f are attributable directly to changes in the rate of moisture entrainment within the wave. Results are presented in the following section.

TABLE 1. Entrainment rates for deep and midlevel convection of the basic-state environmental specific humidity $\overline{q}$ and perturbations from the basic-state q' for particular cases of f and α. Entrainment rates are derived as the coefficients of $\overline{q}$ and q' in (11), assuming that q^c prescribed in the $f = 1.5$, $\alpha = 1/3$ simulation is obtained as $\overline{q}$ from the $f = 1.5$, $\alpha = 0$ case.

Parameter values		Entrainment rate	
f	α	$\overline{q}$	q'
1.0	0	ε	ε
1.5	0	1.5ε	1.5ε
1.5	1/3	1.5ε	ε

4. Results

a. *Effect of varying f, using standard entrainment scheme ($\alpha = 0$)*

Three integrations were performed for $f = 1.0$, 1.5, and 2.0 (with $\alpha = 0$). The mean state—defined as the time and zonal mean—precipitation for each run is shown in Fig. 2a and for 6°N–6°S (over which range more than 90% of the model precipitation is from the convection scheme) in Fig. 2b, which covers most of the width of the ITCZ. The mean precipitation varies very little in the extratropics with changing f, as it is only in the tropics that deep and midlevel convection dominate over dynamics. The particular configuration of the model we use has a split ITCZ in the control case, changing to a single, stronger, narrower ITCZ at higher f.

According to Rajendran et al. (2013), about two-thirds of models used in the APE had a single ITCZ with the control SST profile, but other studies have shown that the switch between a single and double ITCZ in an aquaplanet is highly sensitive and depends on the type of convection scheme used and on a variety of parameters (e.g., Lee et al. 2003; Liu et al. 2010; Möbis and Stevens 2012; Oueslati and Bellon 2013). The result found here is consistent with Möbis and Stevens (2012), Oueslati and Bellon (2013), and Talib et al. (2018), who each found a switch from a double to a single ITCZ on enhancing the entrainment rate in an aquaplanet (see section 1). This result is to be expected because as a convective updraft

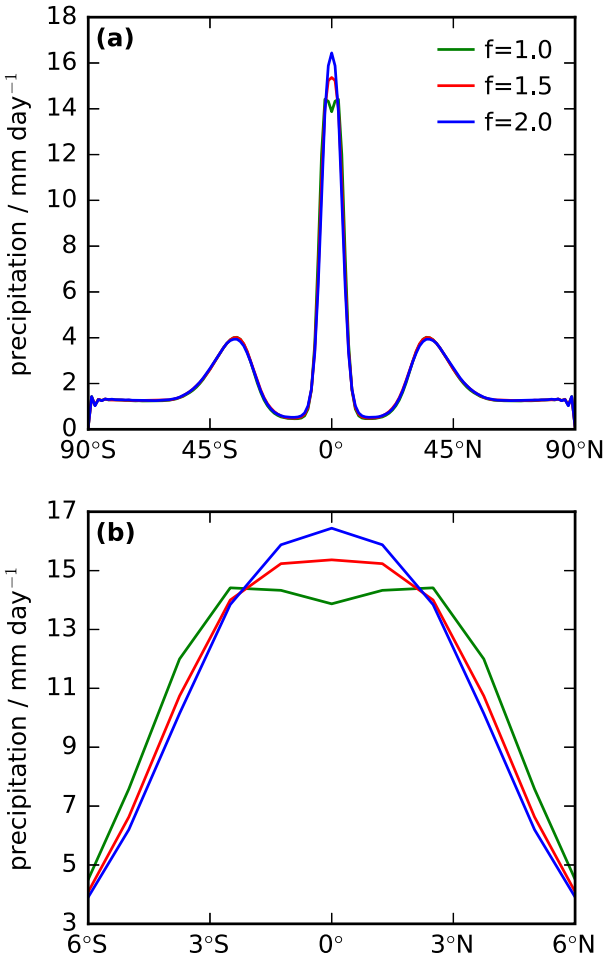

FIG. 2. (a) Time- and zonal-mean precipitation for the experiments with convective entrainment parameter $f = 1.0$, 1.5, and 2.0 and decoupling parameter $\alpha = 0$. (b) As in (a), but zooming in on the ITCZ region only.

rises through the lower troposphere, its humidity reduces, because of entrainment from the environment, as does its buoyancy. If the entrainment rate is increased, then more boundary layer moist static energy (MSE) is required to sustain deep convection [although Talib et al. (2018) show that cloud radiative effects also have an important role in this sensitivity]. Therefore, the ITCZ convection favors warmer SST, which, in these experiments, peaks on the equator [see (1)].

To investigate the effect of entrainment rate on convectively coupled equatorial waves, we compute spectra in zonal wavenumber (k)–frequency (ω) space (Wheeler and Kiladis 1999) of daily mean precipitation. The precipitation time series was separated into 108-day segments, overlapping by 72 days and tapered to zero over 5 days at either end. Each segment was Fourier transformed in time and longitude, and the Fourier coefficients for each segment were summed together. This was performed separately for each latitude ϕ from 15°N to 15°S, then the spectra for each latitude were summed; unlike in Wheeler and Kiladis (1999), at this stage, the spectra were each weighted by $\cos\phi$. The logarithm of this field is plotted in Fig. 3. Unlike Wheeler and Kiladis (1999), we do not first separate the field into its equatorially symmetric and antisymmetric parts. The right-hand side of the plots (positive k) shows eastward-propagating disturbances.

The blue curves are dispersion relations obtained from the standard equatorial wave theory on a resting atmosphere (e.g., Holton 2004) for an equatorial Kelvin wave (eastward propagation, straight line through the origin); equatorial Rossby waves with meridional wavenumber $n = 1, 2$, and 3 (westward propagating, curves through the origin, with $n = 1$ at the top); and a mixed Rossby–gravity wave (extending into both the westward and eastward parts of the diagram). In each case, the curves have been Doppler shifted by the zonal wind from that model run averaged over time, longitude, 15°N–15°S, and 600–400 hPa. These values were −3.73, −2.83, and −2.57 m s^{-1} for $f = 1.0$, 1.5, and 2.0, respectively. The least squares best fit equivalent depth is 85.3 m, obtained by matching the slope for equatorial Kelvin waves in the $f = 1.0$ case after the appropriate Doppler shift had been applied. The same equivalent depth is used for all the theoretical curves.

Figures 3a–c demonstrate that enhancing the entrainment rate increases convectively coupled spectral power—that is, increases the variance of precipitation—across all spatial and temporal scales, consistent with Hirota et al. (2014; see section 1). Thus, the red (stronger at lower ω) background spectrum becomes stronger for larger f. This background partially obscures the wave structures in these diagrams, so it is desirable to remove it. After some experimentation, it was decided to define the background as the spectrum averaged over $k = -15$ to +15. The backgrounds for the three values of f are shown in Fig. 3d. The strongest background power for $f = 1.0$ is at a period of around 27 days, shortening slightly to about 22 days for $f = 2.0$. For $\omega < 0.25$ cycles per day (cpd), the increase from $f = 1.0$ to $f = 1.5$ strengthens the spectrum much more than the increase from $f = 1.5$ to $f = 2.0$. The spectra in Figs. 3a–c were divided by their respective backgrounds (without taking logarithms first), and the ratios are plotted in Fig. 4 with the same dispersion curves as described previously.

For low-ω waves (period of 5 days or more), increasing f results in less Rossby wave power and more Kelvin wave power. Kelvin waves have alternate regions of active and suppressed convection centered on the equator, whereas Rossby waves have off-equatorial convection (Yang et al. 2003). We have already seen

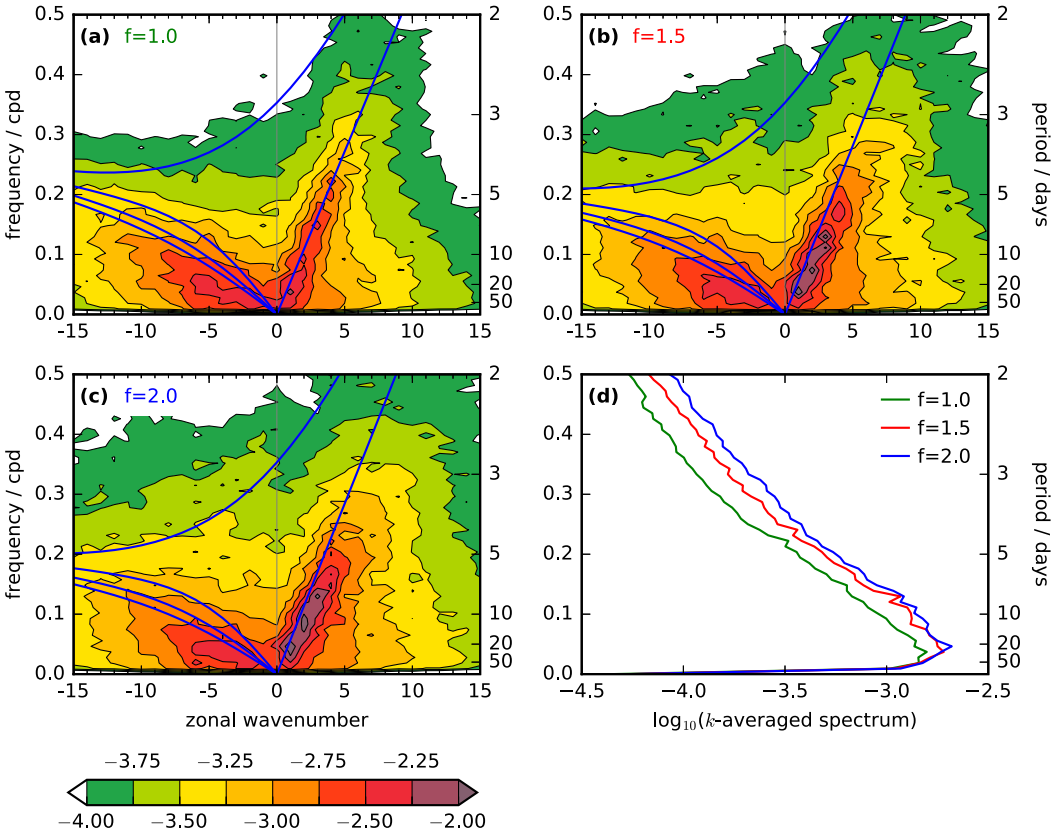

FIG. 3. The $\log_{10}$ of zonal wavenumber–frequency spectral power of precipitation rate for (a) $f = 1.0$, (b) $f = 1.5$, and (c) $f = 2.0$, all with $\alpha = 0$. Blue curves are theoretical dispersion relations for waves with equivalent depth $h = 85.3$ m (see main text for details), Doppler shifted by the mean zonal wind over 15°N–15°S and 600–400 hPa for each model run. (d) Background spectra, defined as the average over $k = -15$ to $k = +15$ of the spectra shown in (a)–(c).

that the ITCZ strengthens and narrows with increasing f, so the changes in Kelvin and Rossby wave power are consistent, with more on-equatorial convection associated with stronger Kelvin waves and less off-equatorial convection associated with weaker Rossby waves. This is consistent with the results of Kang et al. (2013), in which stronger Rossby wave activity was found with a broader peak of SST about the equator (see section 1), which corresponds to our low-f case with broader equatorial convection.

However, this does not hold at higher ω, for which Kelvin waves weaken with increasing f. Furthermore, above 0.3 cpd, the Kelvin wave branch curves upward, especially for $f = 1.0$. This behavior is contrary to the standard theory, in which Kelvin waves are nondispersive (Holton 2004).

We next investigate the sensitivity of the Kelvin wave phase speed c_e to changing f and the role of changes in the basic-state winds (Fig. 5) and humidity (Fig. 6). The Kelvin wave speed, measured by the gradient in k–ω space, reduces with increasing f. However, since the Doppler-shifted dispersion lines in Fig. 4 do not fit the Kelvin waves in the spectra in the enhanced entrainment experiments, this cannot be explained solely by changes in the basic-state zonal wind $\overline{u}$ (Figs. 5a,b,d). Indeed, midlevel easterlies weaken at higher f, so a change in the Doppler shift alone would cause a faster eastward phase speed.

Wang (1988) presented a method for calculating a theoretical value of c_e in a moist environment. Dividing the free troposphere into two levels with midpoints at pressure levels p_1 (upper level) and p_3 (lower level), and the boundary between them at p_2, and letting latent heating be proportional to wave moisture convergence, the theoretical phase speed is[1]

$$c_e = c_0\sqrt{1 - I}, \tag{13}$$

where c_0 is the dry Kelvin wave speed and I is

[1] We change Wang's (1988) α to an A to avoid confusion with our own decoupling parameter.

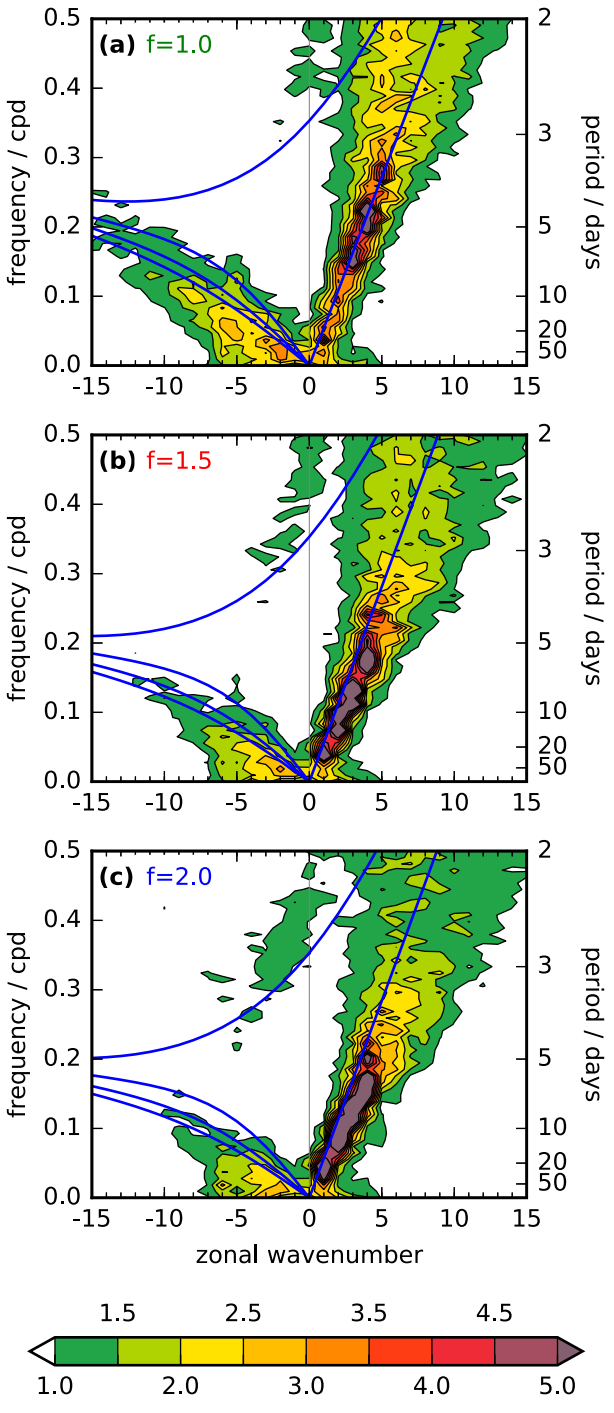

FIG. 4. Wavenumber–frequency spectra with the background removed—that is, the raw spectra shown in Figs. 3a–c divided by the background spectra shown in Fig. 3d (but without taking logarithms first). Blue curves are the dispersion relations described in Fig. 3.

$$I = \frac{\overline{q}_3 - \overline{q}_1}{A}. \tag{14}$$

In (14) $\overline{q}_1$ and $\overline{q}_3$ are the basic-state specific humidity on the equator at the given levels, and

$$A = 2\frac{C_p}{R}\frac{1}{L_c}\frac{p_2}{p_3 - p_1}c_0^2\frac{1}{b}, \tag{15}$$

where $R/C_p = 2/7$ is the adiabatic ratio, $L_c = 2.5 \times 10^6\,\mathrm{J\,kg^{-1}}$ is the specific latent heat of condensation of water, and b is the fraction of moisture converted to precipitation.

This model has only three quantities that may vary with f: the dry wave speed c_0, which depends on static stability; the vertical moisture gradient $\overline{q}_3 - \overline{q}_1$; and the precipitation efficiency b. Choosing $p_1 = 350\,\mathrm{hPa}$, $p_2 = 550\,\mathrm{hPa}$, and $p_3 = 750\,\mathrm{hPa}$, we diagnose the Brunt–Väisälä frequency as

$$N = \sqrt{\frac{g}{\theta_2}\frac{\theta_1 - \theta_3}{z_1 - z_3}}, \tag{16}$$

where z is height, θ is potential temperature, and g is the acceleration due to gravity; N reduces slightly from $0.0118\,\mathrm{s^{-1}}$ ($f = 1.0$) to $0.0117\,\mathrm{s^{-1}}$ ($f = 2.0$), a reduction of 0.8%, contributing a slight reduction in c_0 and slowing the wave. The values of $\overline{q}_3 - \overline{q}_1$ are $8.21\,\mathrm{g\,kg^{-1}}$ for $f = 1.0$, $8.53\,\mathrm{g\,kg^{-1}}$ for $f = 1.5$, and $8.64\,\mathrm{g\,kg^{-1}}$ for $f = 2.0$. Hence, the vertical gradient of $\overline{q}$ strengthens with increasing f (Fig. 6; see section 4b), thus increasing I and also contributing a reduction in c_e. This is because, with more moisture at low levels (upper-level moisture is near zero and varies negligibly between experiments), unit low-level convergence generates more heating, reducing the effective static stability. All else being equal, this reduces $\sqrt{1 - I}$ by 11% from $f = 1.0$ to $f = 2.0$.

The precipitation efficiency b is a convenient quantity in models such as in Wang (1988), but in practice, it is very difficult to diagnose. In principle, it may be measured as the ratio of precipitation rate to vertically integrated moisture flux convergence (VIMFC), averaged over some appropriate time period. However, b is nonconstant given that it depends on variations in q, and in practice for any given value of VIMFC, there is a very broad spread of precipitation rate (e.g., for $f = 1.0$, the correlation coefficient between 5-day means of VIMFC and precipitation is only 0.35). Therefore, it was not possible to diagnose meaningfully a quantitative change in b for increasing f, and predicting the likely change is nontrivial. We can hypothesize that since entrainment dries the plume, increasing f would probably reduce b, thus reducing I and increasing c_e. However, the drying

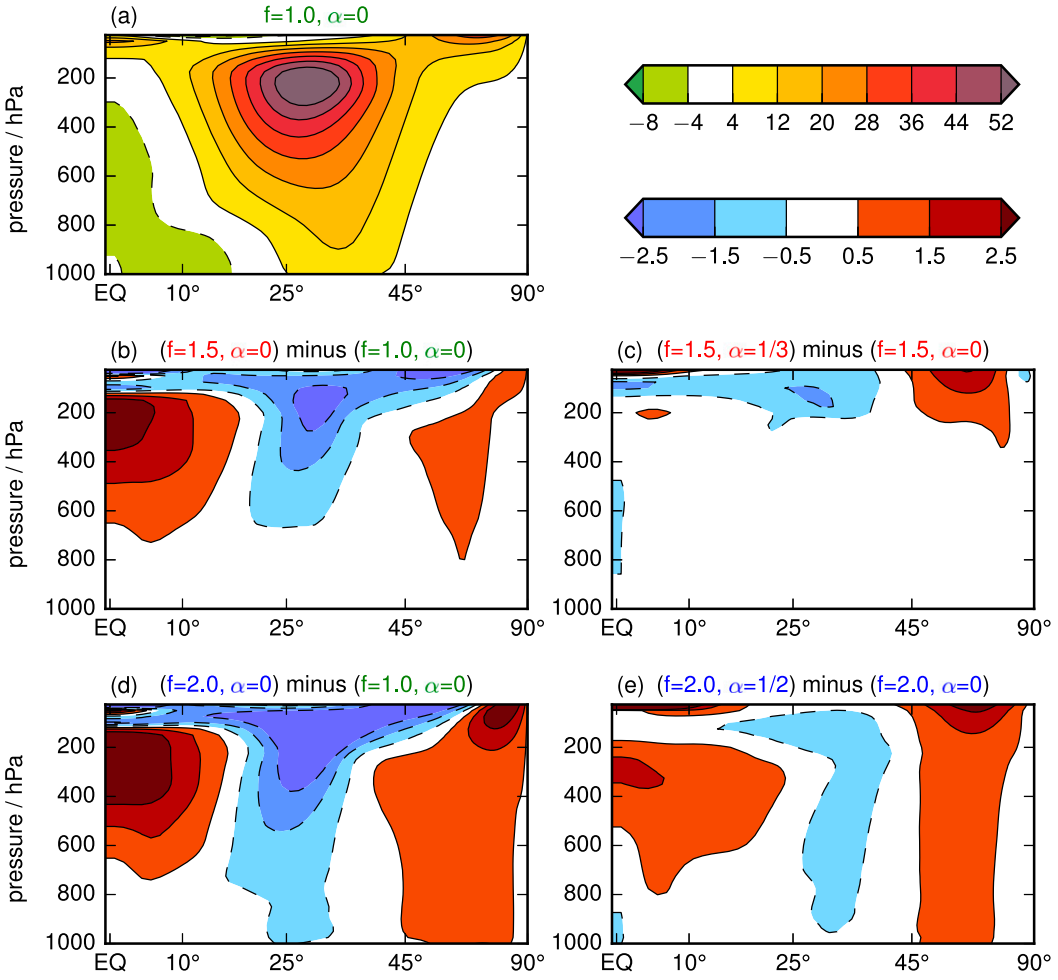

FIG. 5. (a) Time- and zonal-mean (i.e., basic state) zonal wind u (m s^{-1}), for $f = 1.0$, $\alpha = 0$. (b) Difference between $\overline{u}$ for $f = 1.5$ and $f = 1.0$ (both for $\alpha = 0$). (c) For $f = 1.5$, difference between $\overline{q}$ for $\alpha = 1 - 1/f$ and $\alpha = 0$. (d),(e) As in (b) and (c), but for $f = 2.0$ instead of $f = 1.5$. In each case, the fields are averaged over the two hemispheres, and $\sin\phi$ is plotted on the abscissa, with associated latitudes labeled in degrees.

may be offset by the environment being moister at low levels for higher f (Fig. 6). It is also possible that b is affected by changes in vertical structure within the wave; however, the vertical modes arising from the heating profiles in these experiments have negligible changes with varying f (not shown).

When the effect of advection is removed, the measured phase speeds $c_e - \overline{u}$ of the Kelvin waves are 29.0, 23.4, and 21.9 m s^{-1} for $f = 1.0$, 1.5, and 2.0, respectively. This suggests that if the change in b with increasing f does act to speed up the wave, as hypothesized above, the effect must be relatively small since the observed speed reduces. We can say qualitatively, however, that the change in vertical moisture gradient contributes to the change in phase speed—that is, the change in phase speed with changing f depends at least in part on the associated change in basic-state moisture. However, the change in observed phase speed from $f = 1.0$ to $f = 2.0$ is a reduction of 24%, over twice the magnitude of the 11% calculated above. This may be due to effects other than the change in basic-state moisture or shortcomings in the simple Wang (1988) model.

b. *Effect of varying α*

We now consider the effect of changing the decoupling parameter α, as well as f. The three runs in section 4a had $\alpha = 0$, so the moisture entrained was entirely from the environment, and $\overline{q}$ and q' were entrained at equal rates. We now perform runs for $f = 1.5$ and 2.0, with $\alpha = 1/6$, 1/3, 1/2, 2/3, and 1, recalling from section 3 that we are particularly interested in $\alpha = 1 - 1/f$ (i.e., 1/3 for $f = 1.5$; 1/2 for $f = 2.0$).

The mean-state precipitation is shown in Fig. 7, as a difference from the $\alpha = 0$ cases, for 6°N–6°S. Beyond the

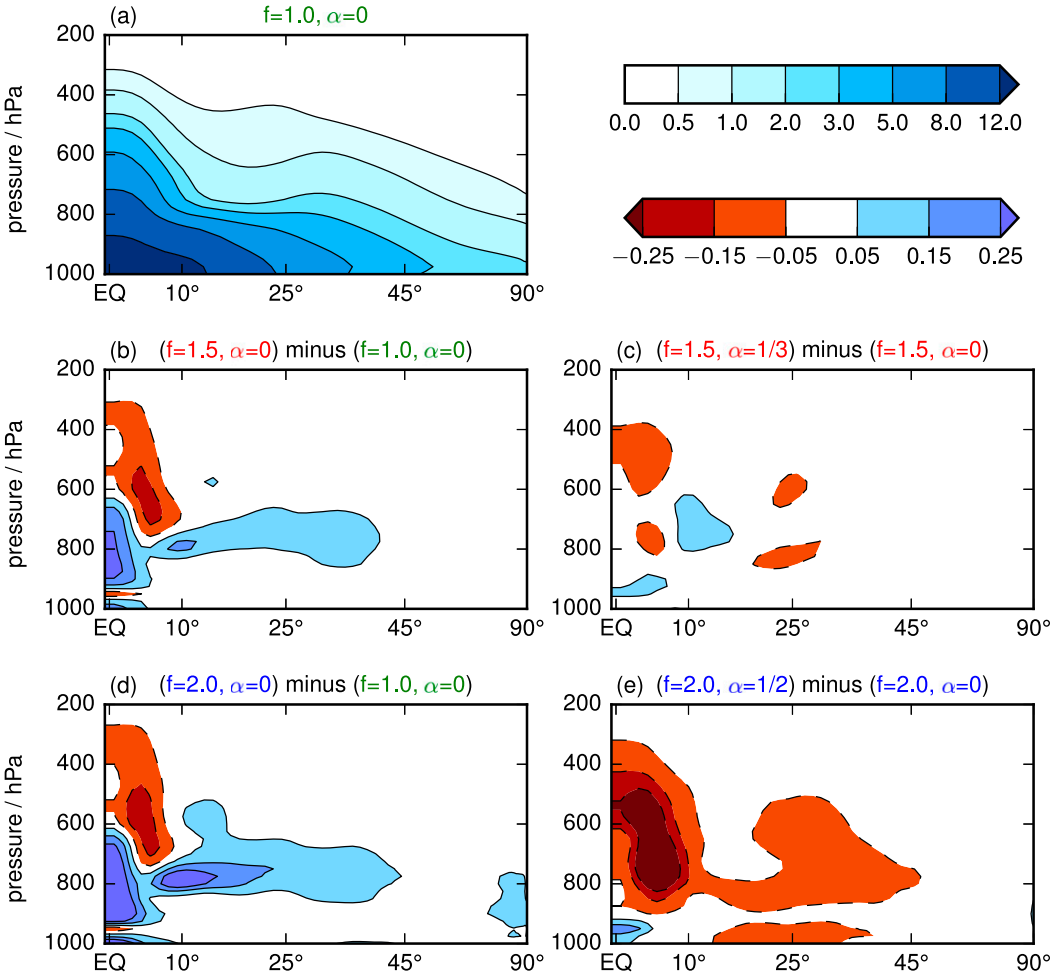

FIG. 6. As in Fig. 5, but for specific humidity q (g kg^{-1}).

tropics, there is almost no perceptible change between experiments. The effect of decoupling from the environment (increasing α) is that the single ITCZ strengthens and narrows. When $f = 1.5$ (Fig. 7a) and $\alpha = 1/6$, precipitation increases by about 1.5 mm day^{-1} on the equator and weakens everywhere poleward of 2°N/S. Increasing α to 1/3 or 1/2 gives much the same ITCZ, but $\alpha = 2/3$ and 1 see a further strengthening at 3°N–3°S, increasing equatorial rainfall by about 2.5 and 4.5 mm day^{-1}, respectively. For $f = 2.0$ (Fig. 7b), increasing α also strengthens near-equatorial rainfall. In contrast to $f = 1.5$, each value of α has well-separated mean precipitation, with $\alpha = 1/6$ giving near-zero change and increasing values giving monotonically increasing amounts of precipitation on the equator. For $\alpha \geq 1/2$, these increases are larger than the equivalents for $f = 1.5$.

Section 3 explained that, in the experimental design, we aimed to minimize the changes in $\overline{q}$ resulting from modifying the entrainment scheme. In particular, we aim to have no change in $\overline{q}$ between the $\alpha = 0$ and $\alpha = 1 - 1/f$ cases for a given value of f.

Figure 6a shows $\overline{q}$ for the control case $f = 1.0$. To eliminate very small meridional asymmetries, the field is averaged over the two hemispheres, and to emphasize the tropics, the horizontal axis is sine of latitude. Figures 6b and 6d show the differences from this control case for $f = 1.5$ and $f = 2.0$, each with $\alpha = 0$. Each shows lower-tropospheric moistening between 4°N and 4°S (approximately the ITCZ region) except for a very thin layer of drier air around 950 hPa, probably associated with changes in boundary layer height. The moistening for higher f is consistent with greater mixing detrainment of moist air out of the plume. It is also possible it could be associated with a change in meridional circulation in line with the changes in the ITCZ (see section 4a), inducing stronger low-level moisture convergence. Above 750 hPa, there are drying regions around 5° off the equator in each

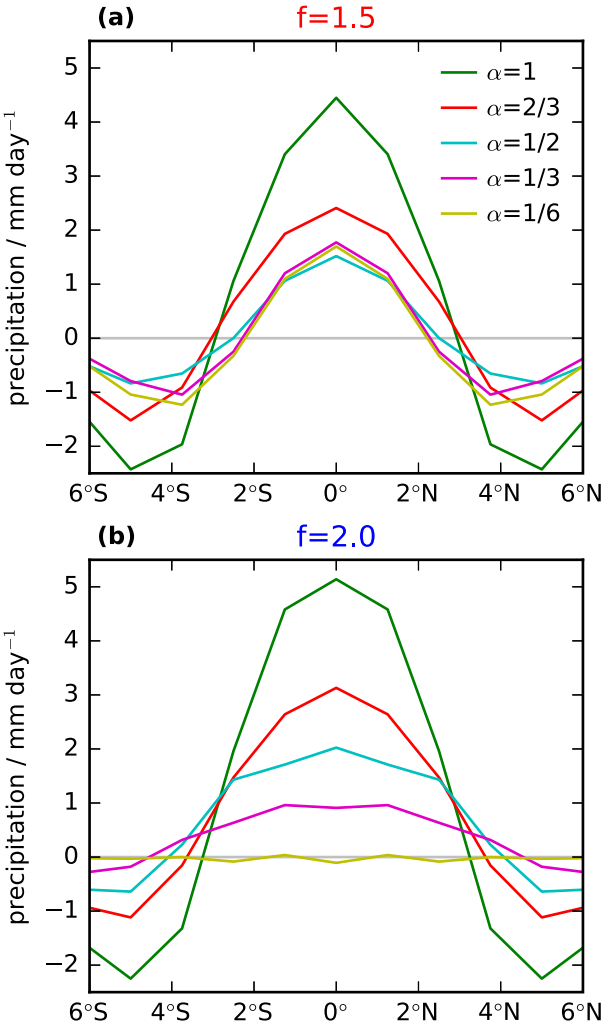

FIG. 7. (a) Time- and zonal-mean precipitation over the ITCZ region for each nonzero value of α used (1/6, 1/3, 1/2, 2/3, and 1) as an anomaly from the $\alpha = 0$ case, for entrainment rate $f = 1.5$. (b) As in (a), but for entrainment rate $f = 2.0$.

hemisphere. This is probably because higher f means more dry air being entrained into the rising plume so that by the time it reaches upper levels it is drier, and less-humid air is detrained back out to the environment. A further layer of increased moisture, centered on 800 hPa and approximately 150-hPa deep, extends beyond the tropics to $\phi = \pm 40°$ for $f = 1.5$ and $\pm 45°$ for $f = 2.0$.

Figures 6c and 6e show $\overline{q}$ for $\alpha = 1 - 1/f$ as differences from the respective $\alpha = 0$ cases. For $f = 1.5$ (Fig. 6c), the difference is near zero, as intended for our experiment, so that (6) and (11) hold approximately. However, for $f = 2.0$ (Fig. 6e), the difference is far greater, with the atmosphere being significantly drier almost everywhere within the tropics. The difference in the equatorial troposphere from the $\alpha = 0$ case is greater than the effect of doubling entrainment in the first place. The tropical off-equatorial region above 750 hPa in which air dried with increasing f strengthens and deepens considerably with increasing α. The regions of enhanced moisture—on the equator in the lower troposphere and extending into the extratropics around the top of the boundary layer—are both considerably weakened. The only region in which increasing α moistens the air is on the equator at 950 hPa, canceling out the drier air that was seen there when increasing f.

Although the experimental design attempted to maintain the basic state in q only, we also consider $\overline{u}$. The control case $f = 1.0$ is shown in Fig. 5a; $\overline{u}$ shows the familiar picture of tropical easterlies and westerly subtropical jets aloft. The effect of enhancing entrainment is seen mainly above 600 hPa, where the jets weaken and, especially for $f = 1.5$, shift marginally equatorward. The easterlies on the equator also weaken in the mid- to upper troposphere. This is likely to be due to a complicated interaction of several effects, including a change in the meridional circulation associated with the change in ITCZ (see section 4a); a change in the propagation of waves from the extratropics to the tropics, which is to be expected with changes to the subtropical jet; and changes to the structure of the equatorially trapped waves. On the latter point, we note that composites of long equatorial Kelvin waves from our experiments (not shown) have a horizontally tilted structure, with $[u^*v^*] > 0$ in the tropical Southern Hemisphere and $[u^*v^*] < 0$ in the tropical Northern Hemisphere (v is meridional wind, square brackets denote a zonal mean, and an asterisk denotes an anomaly from the zonal mean). Therefore, we have negative $(\partial/\partial y)[u^*v^*]$, which contributes eastward acceleration to the mean-state zonal wind (e.g., James 1995), so the change in $\overline{u}$ with increasing f is consistent with the increased Kelvin wave power.

The effect of increasing α to $1 - 1/f$ is seen in Figs. 5c and 5e. As for $\overline{q}$, in the $f = 1.5$ case (Fig. 5c), the effect of α on $\overline{u}$ is near zero, so the basic state is almost unchanged. For $f = 2.0$ (Fig. 5e), there is a reinforcement of the pattern in Fig. 5d, but the effect of increasing α is smaller in magnitude than that of increasing f.

For $f = 2.0$, the entrainment rate is clearly beyond the regime in which our alterations to the convection scheme are able to keep the basic state constant. However, the $f = 1.5$ case works as intended. These results will be borne in mind when we come to compare the $\alpha = 0$ and $1 - 1/f$ cases (section 4c).

Raw (ω, k) spectra of precipitation for all experiments are shown in Figs. 8a–m; f increases going down the figure, and α increases from left to right (Figs. 8a,b,h are the same as those shown in Fig. 3). Decoupling from the

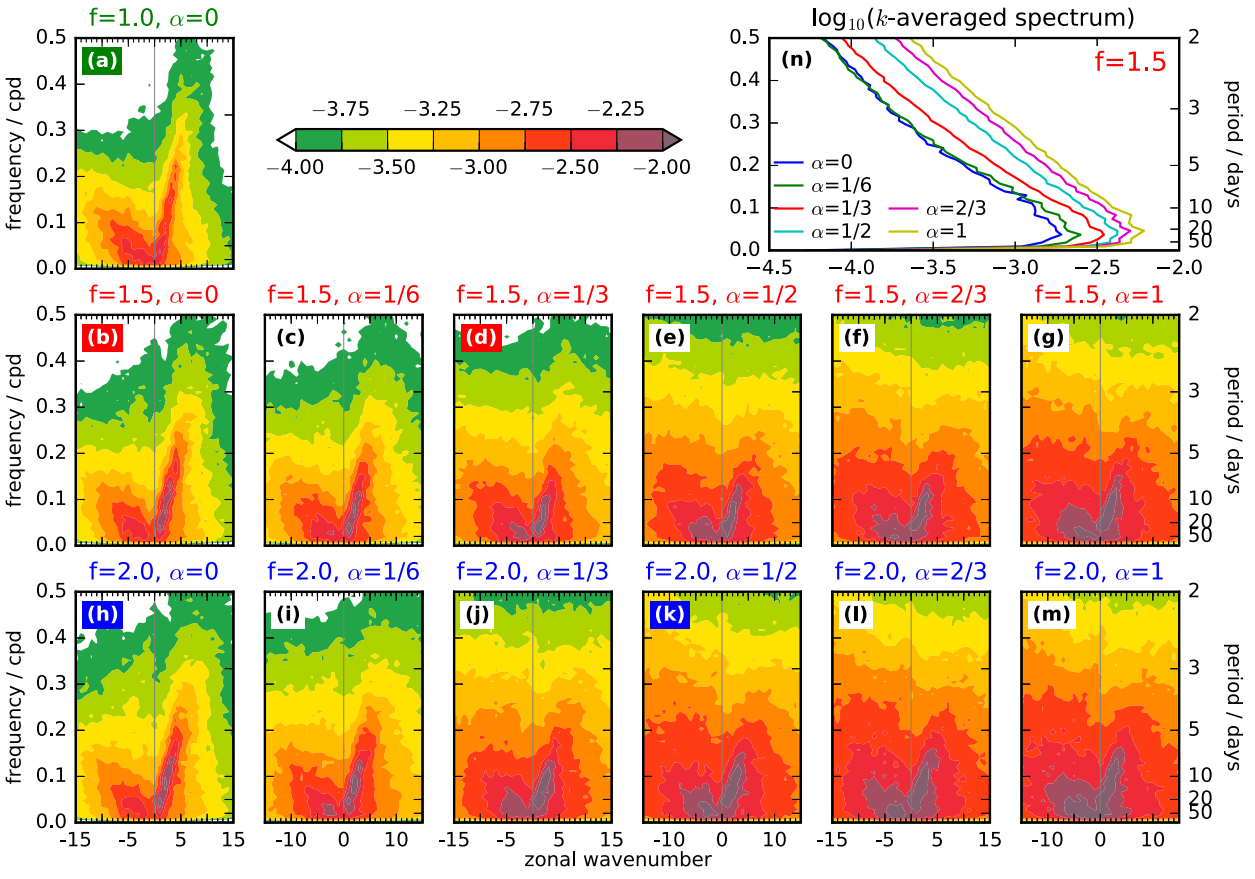

FIG. 8. (a)–(m) The $\log_{10}$ of raw zonal wavenumber–frequency spectra of precipitation for varying entrainment rate f (increasing from top to bottom) and decoupling parameter α (increasing from left to right). Highlighted labels indicate the special cases (a),(b),(h) $\alpha = 0$ and (d),(k) $\alpha = 1 - 1/f$. (n) Background spectra for $f = 1.5$, defined as the average over $k = -15$ to $k = +15$ of the spectra shown in (b)–(g).

environment increases spectral power across all ω and k. Typical 6-h mean snapshots of precipitation are shown in Fig. 9 for $\alpha = 0$ (all values of f), and $\alpha = 1 - 1/f$ and $\alpha = 1$ (f = 1.5 and 2.0). Increasing f results in more concentrated regions of heavy convective rainfall [consistent with Arnold and Randall (2015)]. However, the concentration and intensification is even more marked for increasing α. This is consistent with the changes in the spectra in Fig. 8 as the more sharply defined features of aggregated convection contribute to the spectrum across a broad range of zonal wavenumbers, so there is a large amount of spectral power for large k.

At high ω, for both $f = 1.5$ and $f = 2.0$, the spectra in Fig. 8 are dominated by eastward power for low α (contours sloping upward to the right), yet westward power increases most with increasing α. As in Fig. 3, equatorial waves are obscured by the strong background, which we obtain by averaging over $k = -15$ to $+15$ (shown for $f = 1.5$ in Fig. 8n; $f = 2.0$ is very similar). Power increases monotonically with α over all ω and, as with increasing f, increasing α slightly shortens the period at which the spectrum peaks, from 27 days for $\alpha = 0$ to 22 days for $\alpha = 1$.

Ratios of raw spectra to their background are shown in Fig. 10 (Figs. 10a,b,h are the same as in Fig. 4). The clearest effect on convectively coupled waves of increasing α is that short Kelvin waves (high ω and high k) become indistinguishable from the background because of the background becoming stronger, so convection at these time scales is no longer organized into wave structures (consistent with the small-scale aggregated regions seen in Figs. 9f and 9g). Above $\alpha = 1/2$, Kelvin waves of $\omega > 0.25$ cpd are no stronger in spectral power than the background. The ratio of Kelvin wave power to background power at lower ω also decreases with increasing α. For example, for $f = 2.0$, the spectral ratio exceeds 5.0 in almost all of the thin linear region from ($k = 1$, $\omega = 0.025$ cpd) to ($k = 4$, $\omega = 0.175$ cpd) for $\alpha = 0$ (peaking at 10.6 and with a mean of 7.0; Fig. 10h), but for $\alpha = 1$, the mean ratio over the same area is just 2.8 (Fig. 10m). This is despite the total power (Fig. 8), along the entire Kelvin wave branch, varying little with α.

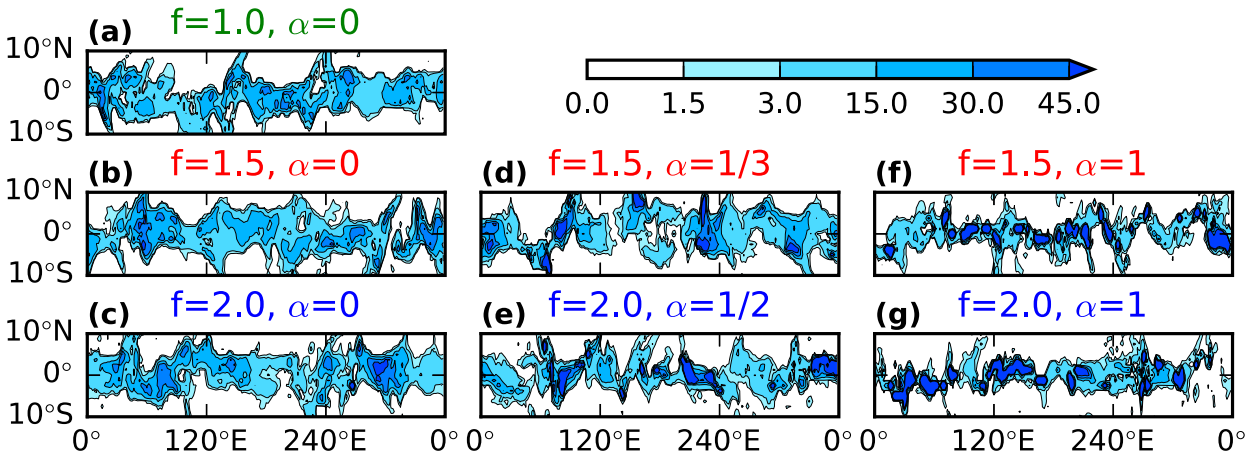

FIG. 9. Example of 6-hourly mean near-equatorial precipitation (mm day^{-1}) for runs with (a)–(c) $\alpha = 0$, (d),(e) $\alpha = 1 - 1/f$, and (f),(g) $\alpha = 1$.

As α increases, entrainment is less strongly coupled to zonal variations in q, and the convectively coupled Kelvin wave power accordingly becomes less prominent against the background, with only the longer (more zonally uniform) waves clearly distinguishable. The shorter convectively coupled waves are indistinguishable from the background when entrainment does not see the wave structure in moisture.

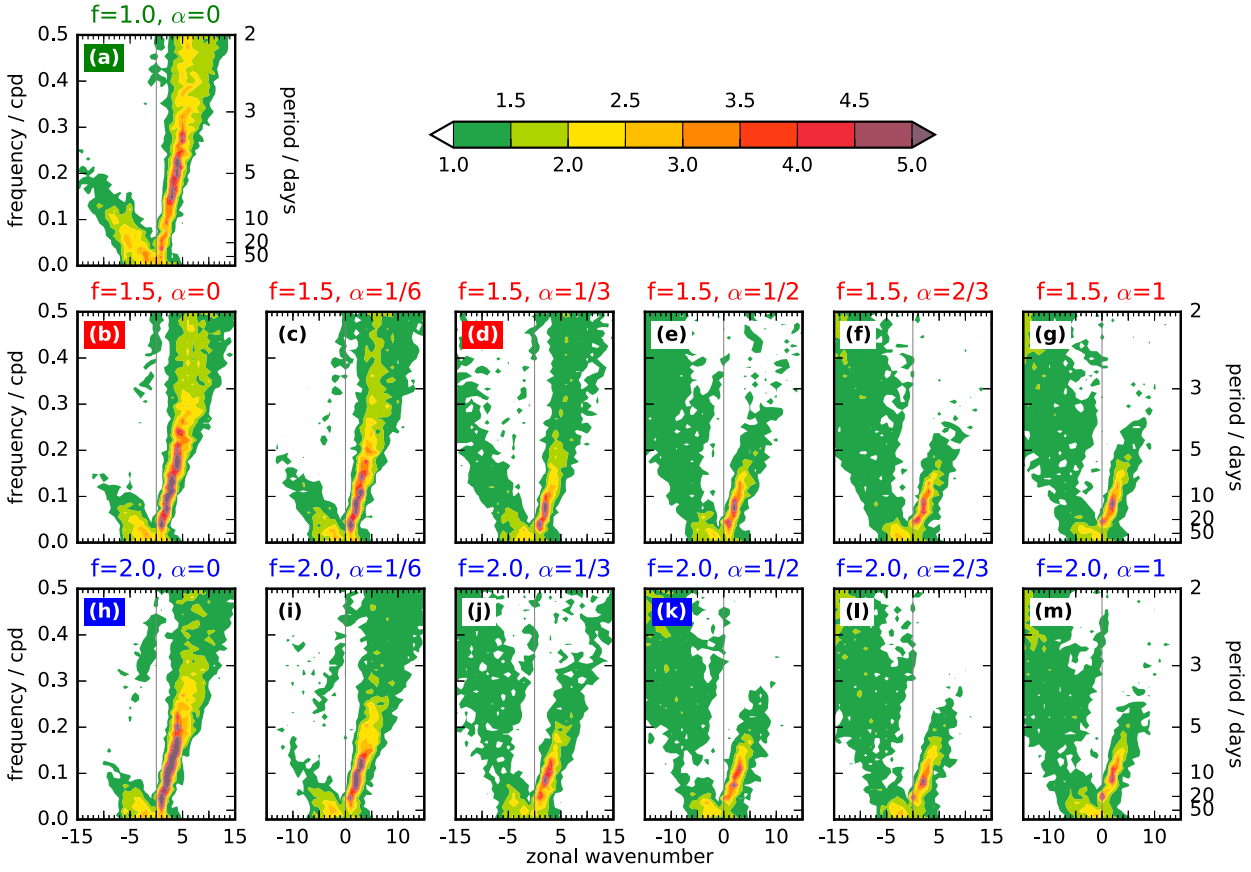

FIG. 10. Wavenumber–frequency spectra with background removed—that is, the raw spectra shown in Figs. 8a–m divided by the background k-averaged spectra (shown for $f = 1.5$ in Fig. 8n). Highlighted labels are as in Fig. 8.

TABLE 2. Summary of the effect on spectral power, as a ratio relative to the background power, of increasing the parameters f and α (see Fig. 10). An up (down)-pointing arrow indicates that the spectral power of waves relative to the background generally increases (decreases) as the given parameter increases.

	Westward power		Eastward power	
Parameter to increase	Low ω, k	High ω, k	Low ω, k	High ω, k
f	↓	↓	⇑	↓
α	↓	⇑	↓	↓

For westward-propagating waves, the ratio also decreases at low ω as α increases, but conversely, for higher ω, the spectral power increases relative to the background. However, it is not presently understood why this is the case.

The effect of varying f and α is summarized for eastward and westward power, for both small ω, k and large ω, k, in Table 2.

c. *Attribution of results to changes in the basic state*

We now turn to the question of whether changes in wave activity with changing f are attributable to the change in entrainment in the moisture wave or to other effects. The previous subsection found (Figs. 5 and 6) that for $f = 1.5$, the basic state is almost unchanged when increasing α from 0 to $1 - 1/f$, as designed. However, for $f = 2.0$, this was not the case, so we cannot draw the same conclusions for the $f = 2.0$ case as for $f = 1.5$.

We return to the (ω, k) spectra of precipitation, relative to the background spectra, in Fig. 10. The panels with highlighted labels contain the important cases of $\alpha = 0$ (Figs. 10a,b,h) and $\alpha = 1 - 1/f$ (Figs. 10d,k). For Fig. 10d, we consider whether the spectrum is most like the respective $\alpha = 0$ case (Fig. 10b) or the $f = 1.0$ case (Fig. 10a). For large ω, the $\alpha = 1 - 1/f$ case is very unlike the $\alpha = 0$ case, and for small ω, they are also not very similar. The eastward power for $f = 1.5$, $\alpha = 1/3$ is weaker than for $f = 1.5$, $\alpha = 0$ and peaks in a different place than for $f = 1.0$ (at less than 0.1 cpd compared with around 0.2 cpd).

Since this comparison does not produce a distinct attribution for changes to the wave activity, we look further by averaging over $k = 1$ to 15 and over $k = -1$ to -15 to examine the mean eastward- (Fig. 11a) and westward-propagating (Fig. 11b) power. We show this for ω up to 0.25 cpd—the region of the spectrum in which most of the power is in the waves—so we may think of this as the eastward- and westward-propagating wave power.

For $\omega < 0.1$ cpd, the eastward power for $f = 1.5$, $\alpha = 1 - 1/f$ is generally closest to the $f = 1.5$, $\alpha = 0$ curve. This is especially true below 0.05 cpd.

For the westward-propagating power, $f = 1.5$, $\alpha = 1 - 1/f$ is closest, and of a similar functional form, to $f = 1.5$, $\alpha = 0$, up to around 0.2 cpd. Therefore, in a k-averaged sense, the changes in wave activity we see with increasing f cannot be directly explained by changes in moisture entrainment in the wave, since $\alpha = 1 - 1/f$ bears the most resemblance to $\alpha = 0$ with the same f despite these two cases entraining q' at different rates.

A clearer picture still is obtained from the ratio of eastward-to-westward power (Fig. 11c). For $\omega < 0.085$ cpd (period $\gtrsim$12 days), the $f = 1.5$, $\alpha = 1 - 1/f$ case is very similar to $f = 1.5$, $\alpha = 0$. Nowhere does the $\alpha = 1 - 1/f$ resemble $f = 1.0$. Therefore, the change in the ratio of eastward-to-westward power for low ω and k as f increases from 1.0 to 1.5 is again not explained directly by changes in moisture entrainment in the wave but must be attributed to other impacts of varying entrainment rate, which includes a change of basic state. As explained in section 1, Kang et al. (2013) made an argument for the basic state affecting the ratio of eastward-to-westward power of convectively coupled equatorial waves. In this study, we have provided evidence that when the entrainment rate is varied, the direct impact does not explain such a change in wave activity, consistent with the theory that instead changes in basic state (as seen in Fig. 6; see section 4b) are responsible.

5. Conclusions

This study was motivated by the known impact of varying moisture entrainment rate on convectively coupled tropical waves, particularly in the context of MJO propagation. Any new feature or configuration change in a GCM is liable to impact the basic state, which itself may impact the modeled physical processes. It is generally nontrivial to distinguish the direct impact of a change in model physics from indirect impacts such as altering the basic state. In this paper, we have presented a novel framework with the aim of isolating these effects for the case of a change in moisture entrainment affecting convectively coupled equatorial waves.

Following Klingaman and Woolnough (2014), experiments were conducted with the entrainment rate for deep- and midlevel convection at the control level for the GA3 configuration of the MetUM ($f = 1.0$) and with the entrainment rate increased by 50% ($f = 1.5$) or 100% ($f = 2.0$). These experiments (Figs. 2–4) showed a tendency toward a single, stronger ITCZ with increasing f and an increase in spectral power of precipitation across all ω and k (i.e., the background became stronger).

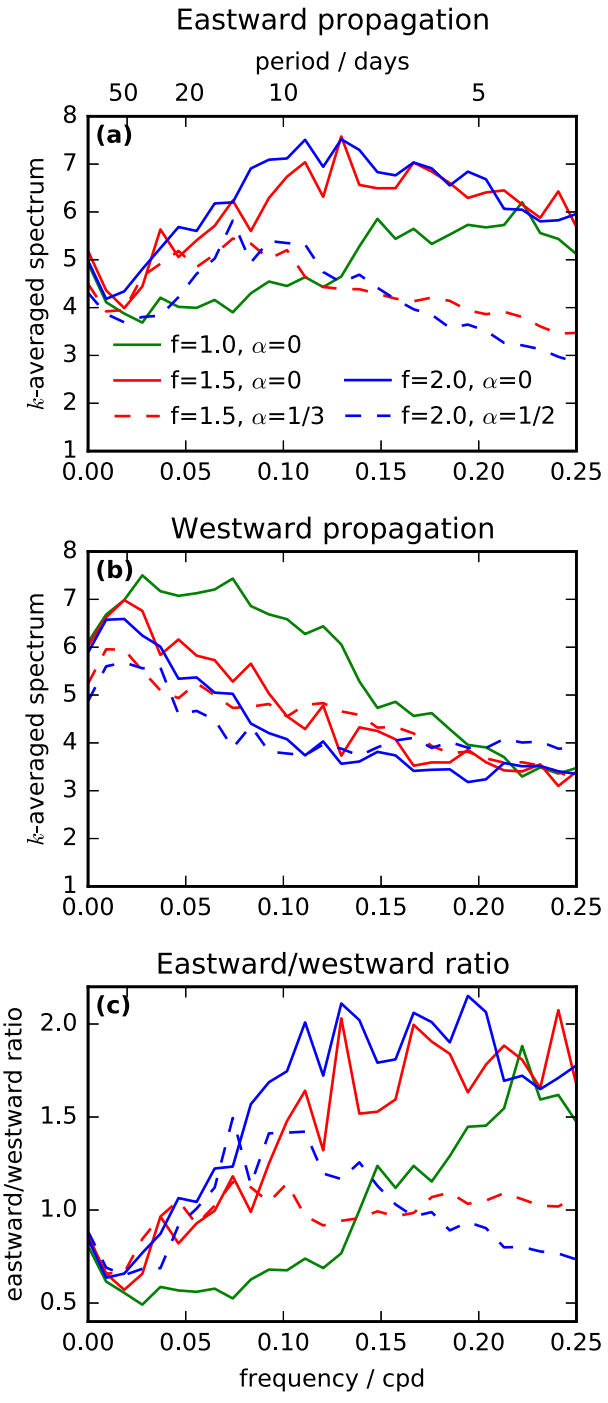

FIG. 11. (a) Averages of each of the five highlighted spectra in Fig. 10 for $k = +1$ to $k = +15$ (i.e., power in the eastward half of the spectrum). (b) As in (a), but for $k = -1$ to $k = -15$ (i.e., westward power). (c) Ratio of (a) to (b). The $\alpha = 0$ cases are plotted with solid lines and $\alpha = 1 - 1/f$ with dashed lines; $f = 1.0$ is shown in green, $f = 1.5$ in red, and (for reference) $f = 2.0$ in blue.

For equatorial Kelvin waves, increasing f increased power in long waves and reduced power in short waves. Wang (1988) predicted that, provided $I < 1$ and $2\overline{q}_{\mathrm{BL}} - \overline{q}_3 - \overline{q}_1 > A$ [where $\overline{q}_{\mathrm{BL}}$ is $\overline{q}$ at the top of the boundary layer and the other symbols have the same meanings as in (14)], Kelvin waves can be unstable. Both of these inequalities hold in our experiments. Furthermore, Wang (1988) predicted that long waves become unstable first as the left-hand side of the second inequality increases, with a short-wave cutoff. Taking the pressure at the top of the boundary layer to be 900 hPa, we can confirm that $2\overline{q}_{\mathrm{BL}} - \overline{q}_3 - \overline{q}_1$ does increase with f (15.80 g kg^{-1} for $f = 1.0$, 16.10 g kg^{-1} for $f = 1.5$, and 16.38 g kg^{-1} for $f = 2.0$), so our results are consistent with this prediction.

Enhancing the entrainment rate reduced the ratio of the power in westward-propagating (e.g., Rossby) waves to the power in the background, because of the background strengthening. It also reduced the ratio of power relative to the background for eastward-propagating waves at high ω and k but increased the ratio for low ω and k. This is consistent with Kang et al. (2013), who investigated changes in wave power due to changing the prescribed meridional SST gradient through its effect on the meridional gradient of $\overline{q}$. Here, we do not vary SST, but the $\overline{q}$ gradient is affected by changes in f (Fig. 6), with larger f causing low-level $\overline{q}$ to be more strongly peaked on the equator. This corresponds to Kang et al.'s (2013) narrower SST profile, with narrower equatorial convection; as in our experiment, this caused a decrease in the ratio of Rossby to Kelvin wave power. Gonzalez and Jiang (2017) showed, using 21 GCMs, a positive correlation between model low-level moisture and MJO skill, with better MJO models tending to have a stronger meridional moisture gradient on the equator. The equatorial moistening of the lower troposphere seen with enhanced f in Fig. 6 may therefore explain the results of Klingaman and Woolnough (2014), in which enhanced entrainment improved MJO skill in the MetUM.

The decoupling parameter α was introduced in a new framework designed to separate out the effects of changing the basic state from the direct effect of changing moisture entrainment (section 3). When $\alpha = 0$, the moisture entrainment behaves as normal, entraining moisture from the full three-dimensional humidity field (the environment). However, when $\alpha = 1$, the moisture is entrained from a prescribed climatology, which we take from the time and zonal mean of a previous run with the same value of f and with $\alpha = 0$. When $0 < \alpha < 1$, the moisture entrained is a weighted average of the two fields. We compare experiments with $\alpha = 1 - 1/f$ to $f = 1.0$, $\alpha = 0$, with the enhanced entrainment rate $f\varepsilon$ in

the $\alpha = 1 - 1/f$ case applying to the basic-state humidity $\overline{q}$ only, and humidity perturbations q' being entrained at the control rate ε in both experiments. We also compare experiments with $\alpha = 1 - 1/f$ to $\alpha = 0$ (with the same value of f in each case) since $\overline{q}$ is entrained at rate $f\varepsilon$ in both experiments but humidity perturbations q' are entrained at the control rate ε for $\alpha = 1 - 1/f$. This argument requires the basic state to remain unchanged by the change in α. For $f = 1.5$, the attempt to leave the basic state unchanged works well, with $\overline{q}$ (Figs. 6b,c) and zonal-mean zonal wind $\overline{u}$ (Figs. 5b,c) changing minimally for these values of α. However, for $f = 2.0$, the basic state changes significantly. Therefore, we cannot make any definitive conclusions for the $f = 2.0$ case, but we can be confident in the results when $f = 1.5$.

Increasing α strengthens and narrows the ITCZ (Fig. 7) and increases the background spectrum across all ω and k (Fig. 8). Removing the background spectrum shows that decoupling moisture entrainment from the environment reduces the relative power in the eastward half of the spectrum (Fig. 10). Above 0.25 cpd, it decreases markedly with increasing α as the background spectrum increases. This shows that zonal variations in moisture, to which the entrainment is less sensitive with increased α, are essential for convection to be organized in short Kelvin wave structures. That is, coherent Kelvin wave propagation at high ω and k requires the wave structure to be fully coupled to the moisture field, and this effect is more pronounced for $f = 2.0$ than 1.5. Conversely, only the long Kelvin waves can couple coherently to convection when α is high and the moisture field is more zonally symmetric. Nonetheless, relative power in these long waves does weaken when α increases (Fig. 10), so the wave structure in the humidity field is still important for them, but entrainment of mean humidity is enough to maintain some convectively coupled long Kelvin wave activity.

The mean spectral power for the eastward and westward parts of the spectrum, and the ratio of the two, were shown in Fig. 11. For eastward propagation (which is to say, Kelvin waves), the $\alpha = 1 - 1/f$ cases show a significant difference between low and high frequencies, with low-frequency waves having an amount of spectral power fairly similar to that of $\alpha = 0$ and high frequencies having a drop-off in spectral power, which is not seen for $\alpha = 0$. For westward propagation (Rossby waves), there is always a gradual reduction in spectral power with increasing ω, regardless of the values of f and α.

High-frequency Kelvin waves are associated with a high zonal wavenumber or short wavelength. When α increases, so entrainment depends more on q^c, there is less zonal asymmetry in the entrained q (since q^c depends on latitude and height only). Hence, less zonal asymmetry in entrainment reduces the power seen in short Kelvin waves, although there is relatively little effect on long waves.

For the special case of $f = 1.5$, $\alpha = 1/3$, the eastward-to-westward power ratio is much more similar to $f = 1.5$, $\alpha = 0$ than $f = 1.0$, $\alpha = 0$ for low-frequency waves (below 0.085 cpd). Hence, for this part of the spectrum (a band of the spectrum that also includes the MJO), the effect on waves of changing entrainment is not explained directly by changes in entrainment of moisture in the wave. Moreover, we have seen that for higher f, there is a stronger equatorial peak in basic-state humidity (Fig. 6) and an increase in the ratio of eastward-to-westward spectral power, consistent with the theory of Kang et al. (2013). Together, these findings are consistent—for a 50% increase in entrainment rate relative to the control—with the hypothesis stated in section 1 and motivated by Kang et al. (2013). That is, the change in basic state as f varies explains the change in convectively coupled equatorial wave activity in terms of the eastward-to-westward ratio of wave power. (However, in this setup, it was not possible to test the same hypothesis for a 100% increase in the entrainment rate.)

The mechanism by which the entrainment rate affects the MJO, as found by other studies (see section 1), may similarly be an indirect effect. This would be consistent with the results of Gonzalez and Jiang (2017), in which MJO fidelity depends on low-level mean-state meridional humidity gradient, and Kang et al. (2013), in which the amount of eastward activity relative to the amount of westward activity is dependent on the basic state generated by varying the prescribed SST. Such a finding would also be consistent with MSE hypotheses of MJO propagation (e.g., Wang et al. 2017; Sobel et al. 2014).

Acknowledgments. The project was funded by Natural Environment Research Council (NERC) Grant NE/I012419/1. SJW was also supported by the National Centre for Atmospheric Science, an NERC collaborative center, under Contract R8/H12/83/001. This work used the ARCHER U.K. National Supercomputing Service (http://www.archer.ac.uk). The authors are grateful to Dr. Nick Klingaman for access to model output that motivated this work and for assistance in running the MetUM, to Dr. Stephanie Johnson for guidance in editing the code of the MetUM convection scheme, and to Dr. Michael Whittall for helpful advice regarding the modifications to the convection scheme. We thank three anonymous reviewers whose comments helped us strengthen and clarify the arguments of this paper. The source code for the MetUM is available to use. A license for the MetUM can be applied for online (https://www.metoffice.gov.uk/research/collaboration/um-partnership).

For more information on the exact model versions and branches applied, please contact the authors. Data from the simulations are archived at the Met Office and available for research use through the Centre for Environmental Data Analysis JASMIN platform (http://www.jasmin.ac.uk); please contact the authors for details.

APPENDIX

Discretization of Convection Scheme Equations in the MetUM

a. Implementation of the new moisture entrainment framework

In section 3, modifications to the MetUM convection scheme were introduced that change the moisture entrained into a plume [(7)]. These changes are implemented in the model as follows. The pertinent equations in the convection scheme are, from Gregory and Rowntree's (1990) (6) and (8) (and using their notation throughout),

$$\frac{\partial M_P}{\partial \sigma} = E - N - D, \tag{A1}$$

and

$$\frac{\partial q^P M_P}{\partial \sigma} = Eq^E - Nq^N - Dq^R - Q, \tag{A2}$$

where M_P is the cloud mass flux; σ is the vertical coordinate; E is the entrainment rate; N is the mixing detrainment rate; D is the forced detrainment rate; q^P, q^E, q^N, and q^R are the specific humidity of cloudy air, of the environment, on mixing detrainment, and on forced detrainment, respectively; and Q is the conversion of water vapor to the liquid or ice phase.

In the MetUM, during a call to the convection scheme, the entrainment is performed alone and the detrainment and condensation subsequently. Therefore, as we proceed, we let $N = D = 0$. The above equations are vertically discretized with levels labeled as $K, K+1, \ldots$, with the level number increasing downward in the atmosphere. Entrainment takes place at levels $K-1/4$ and $K-3/4$. Defining the fractional entrainment rate as $\varepsilon = E/M_P$, (A1) and (A2) are discretized as

$$M_{K-1} = M_K + \varepsilon_{K-1/4} M_K \Delta\sigma_{K-1/4} + \varepsilon_{K-3/4} M_K (1 + \varepsilon_{K-1/4}\Delta\sigma_{K-1/4})\Delta\sigma_{K-3/4}, \tag{A3}$$

and

$$M_{K-1}q^P_{K-1} = M_K q^P_K + \varepsilon_{K-1/4} M_K q^E_K \Delta\sigma_{K-1/4} + \varepsilon_{K-3/4}(1 + \varepsilon_{K-1/4}\Delta\sigma_{K-1/4}) M_K q^E_{K-1}\Delta\sigma_{K-3/4}, \tag{A4}$$

where subscripts denote level numbers [cf. (10) and (12) of Gregory and Rowntree 1990].

Substituting (A3) into (A4) yields

$$q^P_{K-1} = \frac{q^P_K + \varepsilon_{K-1/4}\Delta\sigma_{K-1/4}\overbrace{q^E_K}^{1} + \varepsilon_{K-3/4}\Delta\sigma_{K-3/4}(1 + \varepsilon_{K-1/4}\Delta\sigma_{K-1/4})\overbrace{q^E_{K-1}}^{2}}{(1 + \varepsilon_{K-1/4}\Delta\sigma_{K-1/4})(1 + \varepsilon_{K-3/4}\Delta\sigma_{K-3/4})}. \tag{A5}$$

In our new framework, we replace the quantities 1 (q^E_K) and 2 (q^E_{K-1}) with ($q^E_K + \Delta q_K$) and ($q^E_{K-1} + \Delta q_{K-1}$), respectively, where Δq_K and Δq_{K-1} are the Δq defined in (8) at levels K and $K-1$.

b. Effect of convection on environmental specific humidity

After convecting, the MetUM calculates the resulting change to environmental specific humidity. In the standard configuration, this change is [from (21b) of Gregory and Rowntree 1990]

$$\Delta q^E_K = \frac{M_K \Delta t}{\Delta\sigma_K}\{(1 + \varepsilon_{K-1/4}\Delta\sigma_{K-1/4})(1 - \delta_K\Delta\sigma_{K-1/2})(1 - \eta_K\Delta\sigma_{K-1/2})(q^E_{K-1} - q^E_K) + \delta_K\Delta\sigma_{K-1/2}(1 - \eta_K\Delta\sigma_{K-1/2})(q^R_K - q^E_K) + \eta_K\Delta\sigma_{K-1/2}(q^P_K - q^E_K) + [\eta_K\Delta\sigma_{K-1/2} + \delta_K\Delta\sigma_{K-1/2}(1 - \eta_K\Delta\sigma_{K-1/2})]l^P_K\}, \tag{A6}$$

where $\delta = D/M_P$ and $\eta = N/M_P$ are the forced and mixing fractional detrainment rates, respectively, and l^P is cloud liquid water. It is important to note the difference between Δq^E in (A6), which is Gregory and Rowntree's (1990) notation for the correction to environmental humidity after convection, and Δq defined in (8), which is the extra humidity entrained in our new entrainment framework.

The first term of (A6) is due to vertical advection of moisture, because of compensating subsidence balancing the updraft in the plume. We need partially to offset this term to take account of the extra humidity Δq_K entrained at levels $K-1/4$ and $K-3/4$. With reference to Fig. 1 of Gregory and Rowntree (1990), we see that we must subtract

$$\left(\frac{\Delta t}{\Delta\sigma_K}\right) M_K \varepsilon_{K-1/4} \Delta\sigma_{K-1/4} \Delta q_K \quad \text{and}$$
$$\left(\frac{\Delta t}{\Delta\sigma_K}\right) M_{K+1/2} \varepsilon_{K+1/4} \Delta\sigma_{K+1/4} \Delta q_K . \tag{A7}$$

Using the fact that

$$M_{K+1/2} = \frac{M_K}{1 + \varepsilon_{K+1/4}\Delta\sigma_{K+1/4}} \tag{A8}$$

(again from their Fig. 1), the extra terms on the right-hand side of (A6) become

$$\Delta q_K^E = \cdots - \frac{M_K \Delta t}{\Delta\sigma_K}\left(\varepsilon_{K-1/4}\Delta\sigma_{K-1/4} + \frac{\varepsilon_{K+1/4}\Delta\sigma_{K+1/4}}{1 + \varepsilon_{K+1/4}\Delta\sigma_{K+1/4}}\right) \times \Delta q_K . \tag{A9}$$

REFERENCES

Agustí-Panareda, A., and A. C. M. Beljaars, 2008: ECMFW's contribution to AMMA. *ECMWF Newsletter*, No. 115, ECMWF, Reading, United Kingdom, 19–27, https://doi.org/10.21957/28vtm6dpt6.

Arnold, N. P., and D. A. Randall, 2015: Global-scale convective aggregation: Implications for the Madden-Julian oscillation. *J. Adv. Model. Earth Syst.*, **7**, 1499–1518, https://doi.org/10.1002/2015MS000498.

Bechtold, P., M. Köhler, T. Jung, F. Doblas-Reyes, M. Leutbecher, M. J. Rodwell, F. Vitart, and G. Balsamo, 2008: Advances in simulating atmospheric variability with the ECMWF model: From synoptic to decadal time-scales. *Quart. J. Roy. Meteor. Soc.*, **134**, 1337–1351, https://doi.org/10.1002/qj.289.

Blackburn, M., and B. J. Hoskins, 2013: Context and aims of the Aqua-Planet Experiment. *J. Meteor. Soc. Japan*, **91A**, 1–15, https://doi.org/10.2151/jmsj.2013-A01.

Bush, S. J., A. G. Turner, S. J. Woolnough, G. M. Martin, and N. P. Klingaman, 2015: The effect of increased convective entrainment on Asian monsoon biases in the MetUM general circulation model. *Quart. J. Roy. Meteor. Soc.*, **141**, 311–326, https://doi.org/10.1002/qj.2371.

Cornforth, R. J., 2013: West African monsoon 2012. *Weather*, **68**, 256–263, https://doi.org/10.1002/wea.2161.

Crum, F. X., and T. J. Dunkerton, 1992: Analytic and numerical models of wave-CISK with conditional heating. *J. Atmos. Sci.*, **49**, 1693–1708, https://doi.org/10.1175/1520-0469(1992)049<1693:AANMOW>2.0.CO;2.

Dunkerton, T. J., and F. X. Crum, 1991: Scale selection and propagation of wave-CISK with conditional heating. *J. Meteor. Soc. Japan*, **69**, 449–458, https://doi.org/10.2151/jmsj1965.69.4_449.

Gill, A. E., 1980: Some simple solutions for heat-induced tropical circulation. *Quart. J. Roy. Meteor. Soc.*, **106**, 447–462, https://doi.org/10.1002/qj.49710644905.

Gonzalez, A. O., and X. Jiang, 2017: Winter mean lower tropospheric moisture over the Maritime Continent as a climate model diagnostic metric for the propagation of the Madden-Julian oscillation. *Geophys. Res. Lett.*, **44**, 2588–2596, https://doi.org/10.1002/2016GL072430.

Grant, A. L. M., and A. R. Brown, 1999: A similarity hypothesis for shallow-cumulus transports. *Quart. J. Roy. Meteor. Soc.*, **125**, 1913–1936, https://doi.org/10.1002/qj.49712555802.

Gregory, D., and P. R. Rowntree, 1990: A mass flux convection scheme with representation of cloud ensemble characteristics and stability-dependent closure. *Mon. Wea. Rev.*, **118**, 1483–1506, https://doi.org/10.1175/1520-0493(1990)118<1483:AMFCSW>2.0.CO;2.

Haertel, P. T., K. H. Straub, and A. Budsock, 2015: Transforming circumnavigating Kelvin waves that initiate and dissipate the Madden–Julian oscillation. *Quart. J. Roy. Meteor. Soc.*, **141**, 1586–1602, https://doi.org/10.1002/qj.2461.

Hall, N. M. J., G. N. Kiladis, and C. D. Thorncroft, 2006: Three-dimensional structure and dynamics of African easterly waves. Part II: Dynamical modes. *J. Atmos. Sci.*, **63**, 2231–2245, https://doi.org/10.1175/JAS3742.1.

Hayashi, Y., 1970: Theory of large-scale equatorial waves generated by condensation heat and accelerating the zonal wind. *J. Meteor. Soc. Japan*, **48**, 140–160, https://doi.org/10.2151/jmsj1965.48.2_140.

Hirons, L. C., P. M. Inness, F. Vitart, and P. Bechtold, 2013a: Understanding advances in the simulation of intraseasonal variability in the ECMWF model. Part I: The representation of the MJO. *Quart. J. Roy. Meteor. Soc.*, **139**, 1417–1426, https://doi.org/10.1002/qj.2060.

——, ——, ——, and ——, 2013b: Understanding advances in the simulation of intraseasonal variability in the ECMWF model. Part II: The application of process-based diagnostics. *Quart. J. Roy. Meteor. Soc.*, **139**, 1427–1444, https://doi.org/10.1002/qj.2059.

Hirota, N., Y. N. Takayabu, M. Watanabe, M. Kimoto, and M. Chikira, 2014: Role of convective entrainment in spatial distributions of and temporal variations in precipitation over tropical oceans. *J. Climate*, **27**, 8707–8723, https://doi.org/10.1175/JCLI-D-13-00701.1.

Holton, J. R., 2004: *An Introduction to Dynamical Meteorology.* 4th ed. Elsevier, 535 pp.

James, I. N., 1995: *Introduction to Circulating Atmospheres.* 1st ed. Cambridge University Press, 422 pp.

Janicot, S., F. Mounier, and A. Diedhiou, 2008: Les ondes atmosphériques d'échelle synoptique dans la mousson d'Afrique de l'Ouest et centrale: ondes d'est et ondes de Kelvin. *Sécheresse*, **19**, 13–22, https://doi.org/10.1684/sec.2008.0115.

Kang, I.-S., F. Liu, M.-S. Ahn, Y.-M. Yang, and B. Wang, 2013: The role of SST structure in convectively coupled Kelvin–Rossby

waves and its implications for MJO formation. *J. Climate*, **26**, 5915–5930, https://doi.org/10.1175/JCLI-D-12-00303.1.

Kiladis, G. N., C. D. Thorncroft, and N. M. J. Hall, 2006: Three-dimensional structure and dynamics of African easterly waves. Part I: Observations. *J. Atmos. Sci.*, **63**, 2212–2230, https://doi.org/10.1175/JAS3741.1.

——, M. C. Wheeler, P. T. Haertel, K. H. Straub, and P. E. Roundy, 2009: Convectively coupled equatorial waves. *Rev. Geophys.*, **47**, RG2003, https://doi.org/10.1029/2008RG000266.

Kim, D., and Coauthors, 2014: Process-oriented MJO simulation diagnostic: Moisture sensitivity of simulated convection. *J. Climate*, **27**, 5379–5395, https://doi.org/10.1175/JCLI-D-13-00497.1.

Klingaman, N. P., and S. J. Woolnough, 2014: Using a case-study approach to improve the Madden–Julian oscillation in the Hadley Centre model. *Quart. J. Roy. Meteor. Soc.*, **140**, 2491–2505, https://doi.org/10.1002/qj.2314.

Lau, K.-M., and L. Peng, 1987: Origin of low-frequency (intraseasonal) oscillation in the tropical atmosphere. Part I: Basic theory. *J. Atmos. Sci.*, **44**, 950–972, https://doi.org/10.1175/1520-0469(1987)044<0950:OOLFOI>2.0.CO;2.

Lee, M.-I., I.-S. Kang, and B. E. Mapes, 2003: Impacts of cumulus convection parameterization on aqua-planet AGCM simulations of tropical intraseasonal variability. *J. Meteor. Soc. Japan*, **81**, 963–992, https://doi.org/10.2151/jmsj.81.963.

Lin, J.-L., and Coauthors, 2006: Tropical intraseasonal variability in 14 IPCC AR4 climate models. Part I: Convective signals. *J. Climate*, **19**, 2665–2690, https://doi.org/10.1175/JCLI3735.1.

Lindzen, R. S., 1974: Wave-CISK in the tropics. *J. Atmos. Sci.*, **31**, 156–179, https://doi.org/10.1175/1520-0469(1974)031<0156:WCITT>2.0.CO;2.

Liu, Y., L. Guo, G. Wu, and Z. Wang, 2010: Sensitivity of ITCZ configuration to cumulus convective parameterizations on an aqua planet. *Climate Dyn.*, **34**, 223–240, https://doi.org/10.1007/s00382-009-0652-2.

Matsuno, T., 1966: Quasi-geostrophic motions in the equatorial area. *J. Meteor. Soc. Japan*, **44**, 25–43, https://doi.org/10.2151/jmsj1965.44.1_25.

Matthews, A. J., 2000: Propagation mechanisms for the Madden-Julian oscillation. *Quart. J. Roy. Meteor. Soc.*, **126**, 2637–2651, https://doi.org/10.1002/qj.49712656902.

——, and J. Lander, 1999: Physical and numerical contributions to the structure of Kelvin wave-CISK modes in a spectral transform model. *J. Atmos. Sci.*, **56**, 4050–4058, https://doi.org/10.1175/1520-0469(1999)056<4050:PANCTT>2.0.CO;2.

Mekonnen, A., C. D. Thorncroft, A. Aiyyer, and G. N. Kiladis, 2008: Convectively coupled Kelvin waves over tropical Africa during the boreal summer: Structure and variability. *J. Climate*, **21**, 6649–6667, https://doi.org/10.1175/2008JCLI2008.1.

Möbis, B., and B. Stevens, 2012: Factors controlling the position of the intertropical convergence zone on an aquaplanet. *J. Adv. Model. Earth Syst.*, **4**, M00A04, https://doi.org/10.1029/2012MS000199.

Mounier, F., G. N. Kiladis, and S. Janicot, 2007: Analysis of the dominant mode of convectively coupled Kelvin waves in the West African monsoon. *J. Climate*, **20**, 1487–1503, https://doi.org/10.1175/JCLI4059.1.

Oueslati, B., and G. Bellon, 2013: Convective entrainment and large-scale organization of tropical precipitation: Sensitivity of the CNRM-CM5 hierarchy of models. *J. Climate*, **26**, 2931–2946, https://doi.org/10.1175/JCLI-D-12-00314.1.

Rajendran, K., A. Kitoh, and J. Srinivasan, 2013: Effect of SST variation on ITCZ in APE simulations. *J. Meteor. Soc. Japan*, **91A**, 195–215, https://doi.org/10.2151/jmsj.2013-A06.

Schreck, C. J., and J. Molinari, 2011: Tropical cyclogenesis associated with Kelvin waves and the Madden–Julian oscillation. *Mon. Wea. Rev.*, **139**, 2723–2734, https://doi.org/10.1175/MWR-D-10-05060.1.

Sobel, A., S. Wang, and D. Kim, 2014: Moist static energy budget of the MJO during DYNAMO. *J. Atmos. Sci.*, **71**, 4276–4291, https://doi.org/10.1175/JAS-D-14-0052.1.

Straub, K. H., and G. N. Kiladis, 2002: Observations of a convectively coupled Kelvin wave in the eastern Pacific ITCZ. *J. Atmos. Sci.*, **59**, 30–53, https://doi.org/10.1175/1520-0469(2002)059<0030:OOACCK>2.0.CO;2.

Talib, J., S. J. Woolnough, N. P. Klingaman, and C. E. Holloway, 2018: The role of the cloud radiative effect in the sensitivity of the intertropical convergence zone to convective mixing. *J. Climate*, **31**, 6821–6838, https://doi.org/10.1175/JCLI-D-17-0794.1.

Tokioka, T., K. Yamazaki, A. Kitoh, and T. Ose, 1988: The equatorial 30-60 day oscillation and the Arakawa-Schubert penetrative cumulus parameterization. *J. Meteor. Soc. Japan*, **66**, 883–901, https://doi.org/10.2151/jmsj1965.66.6_883.

Ventrice, M. J., and C. D. Thorncroft, 2013: The role of convectively coupled atmospheric Kelvin waves on African easterly wave activity. *Mon. Wea. Rev.*, **141**, 1910–1924, https://doi.org/10.1175/MWR-D-12-00147.1.

Vitart, F., S. J. Woolnough, M. A. Balmaseda, and A. M. Tompkins, 2007: Monthly forecast of the Madden–Julian oscillation using a coupled GCM. *Mon. Wea. Rev.*, **135**, 2700–2715, https://doi.org/10.1175/MWR3415.1.

Walters, D. N., and Coauthors, 2011: The Met Office Unified Model Global Atmosphere 3.0/3.1 and JULES Global Land 3.0/3.1 configurations. *Geosci. Model Dev.*, **4**, 919–941, https://doi.org/10.5194/gmd-4-919-2011.

Wang, B., 1988: Dynamics of tropical low-frequency waves: An analysis of the moist Kelvin wave. *J. Atmos. Sci.*, **45**, 2051–2065, https://doi.org/10.1175/1520-0469(1988)045<2051:DOTLFW>2.0.CO;2.

Wang, L., T. Li, E. D. Maloney, and B. Wang, 2017: Fundamental causes of propagating and nonpropagating MJOs in MJOTF/GASS models. *J. Climate*, **30**, 3743–3769, https://doi.org/10.1175/JCLI-D-16-0765.1.

Wheeler, M. C., and G. N. Kiladis, 1999: Convectively coupled equatorial waves: Analysis of clouds and temperature in the wavenumber–frequency domain. *J. Atmos. Sci.*, **56**, 374–399, https://doi.org/10.1175/1520-0469(1999)056<0374:CCEWAO>2.0.CO;2.

——, and H. H. Hendon, 2004: An all-season real-time multivariate MJO index: Development of an index for monitoring and prediction. *Mon. Wea. Rev.*, **132**, 1917–1932, https://doi.org/10.1175/1520-0493(2004)132<1917:AARMMI>2.0.CO;2.

Yang, G.-Y., B. J. Hoskins, and J. M. Slingo, 2003: Convectively coupled equatorial waves: A new methodology for identifying wave structures in observational data. *J. Atmos. Sci.*, **60**, 1637–1654, https://doi.org/10.1175/1520-0469(2003)060<1637:CCEWAN>2.0.CO;2.

——, ——, and ——, 2007a: Convectively coupled equatorial waves. Part I: Horizontal and vertical structures. *J. Atmos. Sci.*, **64**, 3406–3423, https://doi.org/10.1175/JAS4017.1.

——, ——, and ——, 2007b: Convectively coupled equatorial waves. Part III: Synthesis structures and their forcing and evolution. *J. Atmos. Sci.*, **64**, 3438–3451, https://doi.org/10.1175/JAS4019.1.

Zhang, C., 2005: Madden-Julian oscillation. *Rev. Geophys.*, **43**, RG2003, https://doi.org/10.1029/2004RG000158.